Ultrathin Piezoelectric Resonators Based on Graphene and Free-Standing Single-Crystal $BaTiO_3$

Lee, Martin; Renshof, Johannes R.; van Zeggeren, Kasper J.; Houmes, Maurits J. A.; Lesne, Edouard; Šiškins, Makars; van Thiel, Thierry C.; Guis, Ruben H.; van Blankenstein, Mark R.; Verbiest, Gerard J.; Caviglia, Andrea; van der Zant, Herre S. J.; Steeneken, Peter G.

How to cite

LEE, Martin et al. Ultrathin Piezoelectric Resonators Based on Graphene and Free-Standing Single-Crystal $BaTiO_3$. In: Advanced materials, 2022, vol. 34, n° 44, p. 2204630. doi: 10.1002/adma.202204630

This publication URL: https://archive-ouverte.unige.ch/unige:165884

Publication DOI: 10.1002/adma.202204630

ADVANCED MATERIALS
www.advmat.de

Ultrathin Piezoelectric Resonators Based on Graphene and Free-Standing Single-Crystal $BaTiO_3$

Martin Lee, Johannes R. Renshof, Kasper J. van Zeggeren, Maurits J. A. Houmes, Edouard Lesne, Makars Šiškins, Thierry C. van Thiel, Ruben H. Guis, Mark R. van Blankenstein, Gerard J. Verbiest, Andrea D. Caviglia, Herre S. J. van der Zant, and Peter G. Steeneken**

Suspended piezoelectric thin films are key elements enabling high-frequency filtering in telecommunication devices. To meet the requirements of next-generation electronics, it is essential to reduce device thickness for reaching higher resonance frequencies. Here, the high-quality mechanical and electrical properties of graphene electrodes are combined with the strong piezoelectric performance of the free-standing complex oxide, $BaTiO_3$ (BTO), to create ultrathin piezoelectric resonators. It is demonstrated that the device can be brought into mechanical resonance by piezoelectric actuation. By sweeping the DC bias voltage on the top graphene electrode, the BTO membrane is switched between the two poled ferroelectric states. Remarkably, ferroelectric hysteresis is also observed in the resonance frequency, magnitude and *Q*-factor of the first membrane mode. In the bulk acoustic mode, the device vibrates at 233 GHz. This work demonstrates the potential of combining van der Waals materials with complex oxides for next-generation electronics, which not only opens up opportunities for increasing filter frequencies, but also enables reconfiguration by poling, via ferroelectric memory effect.

1. Introduction

Piezoelectric resonators are key components in telecommunications applications. Devices like surface acoustic wave and bulk acoustic wave (BAW) resonators are manufactured in high volume to meet the demands of high-frequency 4G and 5G filters.[1] In particular, free-standing thin film bulk acoustic resonators (FBARs) have been widely adopted as the filter technology of choice for 5G bands. FBAR filters are composed of a thin film of a piezoelectric material sandwiched between electrodes in a capacitor geometry that is suspended over a cavity. The thickness of state-of-the-art FBAR filters needs to be reduced to meet the requirements posed by increasing telecom communication frequencies, since resonance frequencies are inversely proportional to thickness. However, scaling down current device geometries is challenging, both because of the complexity of manufacturing such ultrathin suspended heterostructures, but also since the piezoelectric performance[2,3] and breakdown voltage of polycrystalline ceramics diminishes.[4,5] Moreover, realizing uniform electrodes of nanometer-thickness with sufficiently high conductivity and low mass becomes increasingly difficult.

Here, we investigate free-standing crystalline complex oxides as an alternative material platform that can mitigate some of the aforementioned drawbacks and enable resonant filters with improved performances. Single crystals are known to have larger dielectric breakdown voltages compared to their polycrystalline counterparts[6] while materials like BTO and $PbZr_xTi_{1-x}O_3$ (PZT) provide higher piezoelectric coefficients than commonly used AlN, and can thus handle higher voltages and power densities in the thin film form. Furthermore, single-crystal complex oxides in their ultrathin free-standing form are mechanically robust[7] withstanding large strains up to 8%,[8–10] are flexible enough to allow large curvatures[11] and have already been demonstrated as viable nanomechanical resonators.[12–14] Simultaneously, the electrodes, which also need to be scaled down, must be able to support high-GHz frequencies for 5G and 6G applications. In this regard, graphene is an ideal electrode material. Graphene conducts electricity down to the single atomic layer,[15] has ultra high mobilities,[16,17] is mechanically strong,[18,19] is able to withstand large strains[20] and has been demonstrated to support upto 300 GHz operating frequencies.[21] As a result of this, the use of graphene in various nano-electromechanical systems (NEMS) applications has been widely explored.[22–29] For

M. Lee, J. R. Renshof, K. J. van Zeggeren, M. J. A. Houmes, E. Lesne, M. Šiškins, T. C. van Thiel, M. R. van Blankenstein, A. D. Caviglia, H. S. J. van der Zant, P. G. Steeneken
Kavli Institute of Nanoscience
Delft University of Technology
Lorentzweg 1, Delft 2628 CJ, The Netherlands
E-mail: m.lee-2@tudelft.nl; p.g.steeneken@tudelft.nl
R. H. Guis, G. J. Verbiest, P. G. Steeneken
Department of Precision and Microsystems Engineering
Delft University of Technology
Mekelweg 2, Delft 2628 CD, The Netherlands
The ORCID identification number(s) for the author(s) of this article can be found under https://doi.org/10.1002/adma.202204630.

DOI: 10.1002/adma.202204630

these reasons, single-crystalline piezoelectric films sandwiched between graphene electrodes are a promising alternative device geometry for next-generation resonant filters.

In this work, we combine the high-quality mechanical and electrical properties of few layer graphene electrodes, with the strong piezoelectric performance of atomically engineered free-standing complex oxide, $BaTiO_3$ (BTO), to create piezoelectrically actuated resonators with unprecedented thinness. With van der Waals (vdW) assembly techniques we create a capacitor geometry of graphene/BTO/graphene suspended over a cavity in SiO_2/Si. We demonstrate that the device can not only be driven piezoelectrically, but also optothermally and electrostatically, which allows a direct comparison between these actuation techniques. When the DC voltage across the system is swept back and forth, we observe hysteresis in the resonance frequency, Q factor, magnitude and phase, which all point toward ferroelectric polarization switching, providing additional evidence that the actuation is of a piezoelectric nature, and offering a route toward programmable filters. Additionally, using the picosecond ultrasonics technique we verify the BAW mode frequency to be 233 GHz. This work thus opens a door to the next-generation high-frequency piezoelectric actuators with tunable frequencies and reconfigurable polarization states.

2. Results and Discussion

Free-standing BTO thin films are prepared by a combination of a reflection high-energy diffraction assisted pulsed laser deposition (PLD) and water etching. First, a 9 nm thick crystalline sacrificial layer of $Sr_2Al_3O_6$ (SAO) is grown on a TiO_2-terminated $SrTiO_3$(001) substrate. We then grow in situ a single-crystalline thin film of BTO (see Experimental Section for details). The SAO layer serves as a water soluble sacrificial layer for the release of the BTO from the substrate.[30] The high-quality crystalline heterostructure is then characterized using X-ray diffraction (XRD) before and after exfoliation in water. The XRD data are presented in the Section S1, Supporting Information. Afterward, a piece of poly(dimethylsiloxane) (PDMS, gelPak) is attached to the surface of BTO and the sample is submerged under water for 24 h for the etching of the SAO layer. Once the BTO film is released from the growth substrate, it is transferred onto a dummy SiO_2/Si substrate using the deterministic transfer method[31] for further XRD characterization. From the XRD spectra analysis, we obtain a c-axis parameter of 4.085 Å and a thickness of 36 unit cells (u.c.) equivalent to ≈14.7 nm, in the free-standing BTO. We hypothesize that the slightly larger c-axis lattice parameter, compared to the literature value of 4.036 Å[32] may be attributed either to the presence of oxygen vacancies, or to stress applied during the stamping process. A total of three devices, noted device 1, device 2, and device 3 are presented in this work, all fabricated from the same parent film of BTO.

We further assess the ferroelectric properties of our free-standing BTO films using piezoresponse force microscopy (PFM). PFM is performed on an isolated flake transferred on top of a pre-patterned gold electrode. The hysteresis seen in the PFM data confirms the ferroelectricity of free-standing BTO (see Section S2, Supporting Information). The d_{33} and coercive field of the BTO flake are determined to be ≈7 pm V^{-1} and ≈580 kV cm^{-1} respectively, in good correspondence with literature values for ultrathin BTO.[3,33]

After confirming the crystallinity and ferroelectricity of the free-standing BTO, we assemble sandwiches of graphene and BTO flakes into a suspended capacitor geometry for piezoelectric actuation. The heterostructure consists of a multilayer of graphene (16 nm) transferred onto a pre-patterned cavity in SiO_2/Si using a PDMS transfer method,[31] a BTO flake transferred atop using a polymer assisted transfer technique[34,35] and finally a thinner (5 nm) capping layer of top graphene transferred using the PDMS transfer method. The thicknesses of the two multilayer graphene electrodes are intentionally chosen to be asymmetric to introduce a preferential bending moment that drives the heterostructure when the piezoelectric layer expands. Furthermore, the heterostructure has the thicker graphene on the bottom in order to ensure that the electric field from the top graphene is screened by the bottom graphene electrode, to prevent it from contributing to an electrostatic actuation force. An optical image of device 1 is shown in **Figure 1**a with the graphene layers outlined in dashed black lines and BTO in dashed green lines. The pre-patterned substrate consists of Pd/Ti contacts embedded into the SiO_2, surrounding a 285 nm deep circular cavity with a diameter of 8 μm.

The vibrations of the heterostructure membrane are measured at room temperature at a pressure of 10^{-5} mbar using a laser interferometry setup (see Experimental Section and Section S3, Supporting Information). The setup enables three different actuation methods as illustrated in Figure 1b–d. The first method is optothermal driving using an intensity modulated blue (λ = 405 nm) laser (Figure 1b). The second method is electrostatic actuation using the doped Si substrate. As illustrated in Figure 1c, the AC drive signal is applied to the p-doped Si while both the top and bottom graphene flakes are grounded such that there is effectively no electric field across the BTO layer and the actuation is purely dominated by the electrostatic attraction between the bottom graphene and the Si. A small DC voltage of V_{DC} = −1 V is added to the AC drive signal using a bias tee. Finally, piezoelectric actuation is realized by applying the drive signal to the top of the heterostructure while grounding the bottom graphene and the Si substrate (Figure 1d). Here, there is an electric field across the BTO film, between the two graphene layers. The high frequency electric field is able to piezoelectrically actuate the heterostructure into motion. The resulting resonance peak for each driving method, taken at an actuation voltage of V_{AC} = 100 mV are shown in Figure 1b–d (bottom row). The presented device geometry thus facilitates the three actuation methodologies, where piezoelectric actuation has the additional advantage that it does not require an on-chip counter electrode across a narrow gap or optical access, and also potentially offers a readout method.

From here on, we focus on the piezoelectric actuation and ferroelectric switching. Similar to a ferromagnet which switches its magnetization direction at the coercive magnetic field, a ferroelectric material switches its polarization direction at the coercive electric field. Using a bias tee, a DC offset is added to the AC driving signal, thereby sweeping the electric field beyond the coercive fields, switching the polarization of the BTO. The circuit used is illustrated in **Figure 2**a. Figure 2b shows the magnitude and phase ϕ of device 1 at V_{DC} = 0 V. Blue

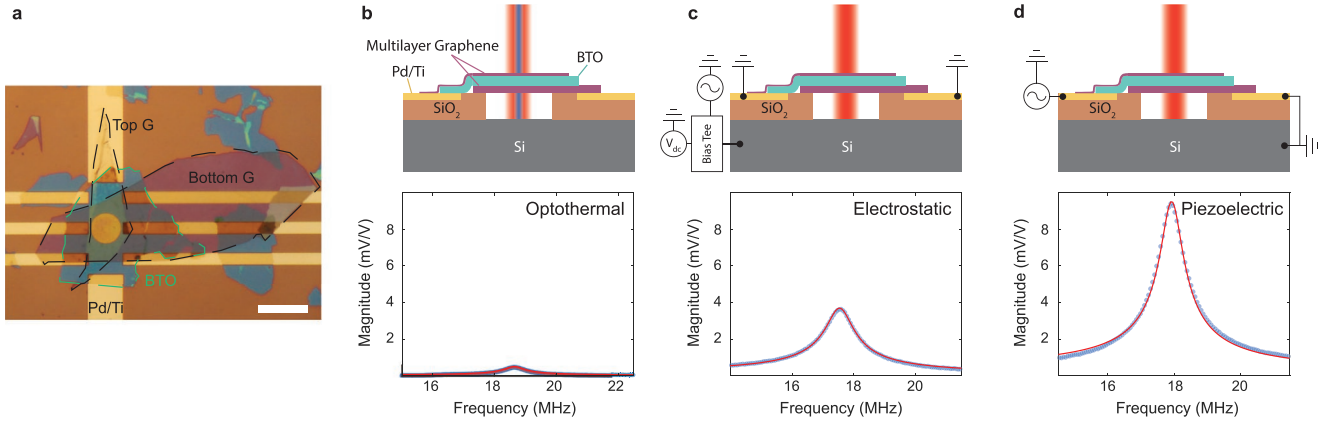

Figure 1. Device geometry and comparison of actuation methods. a) Optical microscopy image of device 1. Top graphene is 5 nm, bottom graphene is 16 nm and BTO is 36 u.c. (≈14.7 nm) thick. Scalebar: 10 µm. b–d) Illustration of the actuation method on top and measured resonance peak using the corresponding actuation method with a 100 mV driving amplitude on the bottom. b) Optothermal driving using an intensity modulated blue ($\lambda = 405$ nm) laser with a power of 93 µW. c) Electrostatic driving with Si substrate while grounding the top and bottom graphene. There is no electric field across the BTO. A DC bias voltage of $V_{DC} = -1$ V is added to V_{AC} using a bias tee. d) Piezoelectric actuation with AC voltage applied to the top graphene while grounding the bottom graphene and the substrate. A red laser ($\lambda = 633$ nm) with a power of 2 mW is used in all three measurements to detect displacements.

plots are taken after first poling the BTO such that its polarization vector points downward (i.e., V_{DC} = 12.5 V) as also illustrated in Figure 2c and the red plots are after first polarizing the BTO upward (i.e., $V_{DC} = -12.5$ V) as illustrated in Figure 2d. As can be seen in Figure 2b, the phase ϕ is different depending on the polarization of the BTO. In particular, ϕ is offset by 180° with respect to the downward polarization when the BTO is polarized in the upward direction. As illustrated in Figure 2c,d, this 180° phase shift can be understood by realizing that when the electric field E_{AC} is parallel to the polarization direction, the BTO expands in the out-of-plane direction while contracting in the in-plane direction. Conversely, when the AC voltage is anti-parallel to the internal polarization, the membrane contracts in the out-of-plane direction while expanding in the in-plane direction in correspondence to the Poisson's ratio. By the alternating voltage V_{AC}, an AC force F_P is generated that drives the membrane into its fundamental mechanical resonance at $f_0 = \omega_0/2\pi$.

The full DC bias response of the device is characterized in **Figure 3**. Unlike the system in the electrostatically driven state (see Section S4, Supporting Information), which shows overlapping forward and backward traces, the system in the piezoelectrically driven state shows hysteresis in f_0, ϕ, Q factor, and magnitude. The observed DC voltage dependence of the electrostatically actuated device is in accordance with previous works on electrostatic actuation.[36,37] Capacitive spring softening of f_0 as well as the linear dispersion of the magnitude are observed. See Section S4, Supporting Information for the full comparison between the DC bias response of the piezoelectrically driven device versus the same device being electrostatically driven.

Figure 3a shows the variation in f_0 while piezoelectrically actuated. The resonance frequency of a circular membrane is described by the following analytical equation[38]

$$f_0 = \frac{2.404}{2\pi r}\sqrt{\frac{Y}{\rho}\frac{S(V_{DC})}{(1-\nu)}} \quad (1)$$

where the prefactor 2.404 arises from the solution to a Bessel function of the first kind, r is the radius of the resonator, Y the Young's modulus, ρ the mass density, $S(V_{DC}) = S_0 + S_{13}(V_{DC})$ the in-plane biaxial strain as a result of the voltage induced piezoelectric stress, S_0 the strain in the membrane at V_{DC}, and ν the Poisson's ratio. The total vertical strain S_{33} in a piezoelectric material when an electric field E_3 is applied between the graphene electrodes is given by[39]

$$S_{33} = Q_{33}P_3^2 + 2Q_{33}\varepsilon_{33}P_3E_3 + Q_{33}\varepsilon_{33}^2E_3^2 \quad (2)$$

where Q_{33} is the electrostriction constant, P_3 the polarization and ε_{33} the dielectric constant. The in-plane strain is related to the out-of-plane strain S_{33} through the Poisson's ratio. When looking at Equation (2), it can be seen that at low values of E_3, the second term, linear in E_3, dominates, with the quadratic term dominating the S_{33} response at larger electric field values. For sufficiently high values of E_3, it can be seen from substituting Equation (2) into Equation (1) that the resonance frequency f_0 is a linear function of $E_3 = V_{DC}/t_{BTO}$ as is visible in Figure 3a in DC bias range from ± 8 V to ± 12.5 V. Normally, the strain in the upward polarization state should have the same strain as the downward state and as a result of Equation (1), upward and downward states should display identical f_0 at V_{DC} = 0 V. However, a noticeable offset between the f_0 of up and down states is observed in Figure 3a. This is due to an initial deflection of the membrane combined with the preferential bending moment facilitated by the asymmetric electrode layers,[40] causing the upward polarization to have a different strain to the downward polarization. As a result, the two polarization states have different resonance frequencies leading to a mechanical memory effect in f_0. In addition to f_0, clear hysteresis in phase, Q-factor and magnitude of the resonance are also observed in Figure 3b–d. The phase ϕ follows a typical hyperbolic tangent profile associated with ferroelectric hysteresis of Ising type[41] (Figure 3b). The coercive field can also be observed

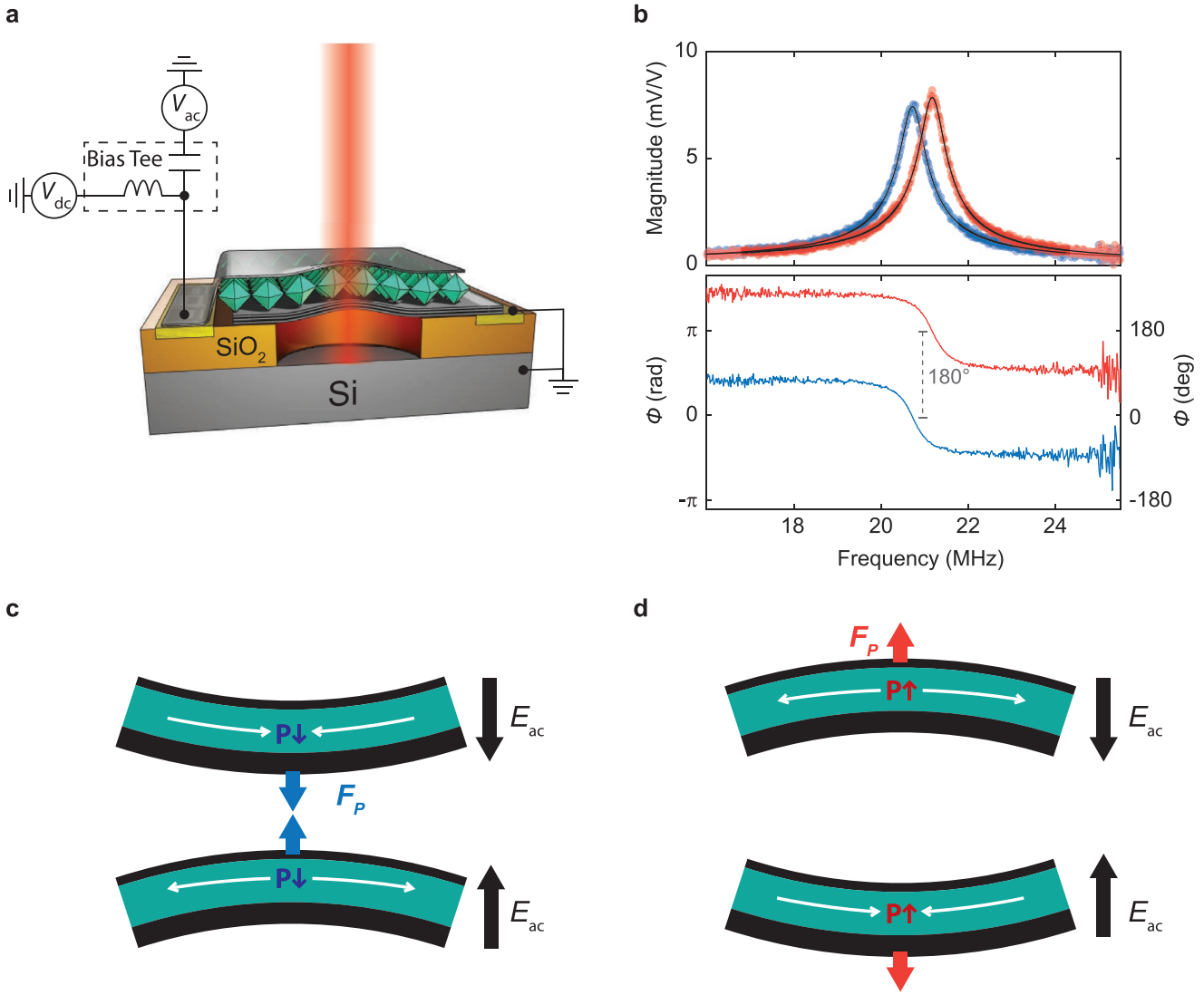

Figure 2. Actuation mechanism of the piezoelectric resonance. a) Illustration of the experimental and device configuration. b) Magnitude (top) and phase ϕ (bottom) of the membrane while sweeping the AC driving frequency of V_{AC}. Red (blue) plots correspond to the measurement performed at V_{DC} = 0 V after poling the device using a negative (positive) bias voltage of V_{DC} = –12.5 V (12.5 V). c,d) Illustration of the actuation mechanism with an instantaneous electric field direction $E_{AC} = E_0\cos(\omega t)$ arising from V_{AC} applied to the top graphene. The direction of the effective piezoelectric force F_P depends both on the polarization direction P after poling and on the instantaneous sign of the externally applied electric field E_{AC} via the voltage V_{AC}. c) Actuation direction of the membrane while the polarization of BTO is pointing downward corresponding to the blue curves in (b). d) Actuation direction of the membrane while the polarization of BTO is pointing upward corresponding to the red curves in (b). The arrows and curves in blue and red colors indicate that an inversion of the polarization direction P causes a 180 ° shift of the phase ϕ of the force on the device. White arrows indicate the in-plane expansion direction.

by analysing the resonance frequency data (see Section S5, Supporting Information).

At the coercive field (i.e., $V_{DC} = V_{coercive}$), P_3 vanishes, which causes the first two terms in Equation (2) to vanish. This is observed in the magnitude (Figure 3c) which shows minima at the positive and negative coercive fields ($V_{DC} = V_{coercive}$ indicated by vertical dashed lines). The inset in Figure 3c shows a representative frequency sweep at V_{DC} = –10.3 V, demonstrating a much smaller magnitude than that at V_{DC} = 0 V shown in Figure 2b. This is also observed at the positive coercive voltage, V_{DC} = 11.2 V. On the other hand, the Q-factor has maxima at the coercive fields. Since the mechanical dissipation is the reciprocal of Q, we find that the dissipation is minimized at the coercive fields. A recent report by Stefani et al.[42] showed that 180° domain walls in ferroelectrics are softer than the domains they separate and thus can reflect energy with little dissipation. Therefore, near the coercive field, where the BTO is in a mixed state with a net zero polarization, the dissipation is expected to be reduced. Furthermore, the overall behavior of the magnitude data qualitatively resembles that of the PFM data of ref. [43] demonstrating a clear correlation between the mechanical vibration of the heterostructure to the piezoelectric properties of the bare film.

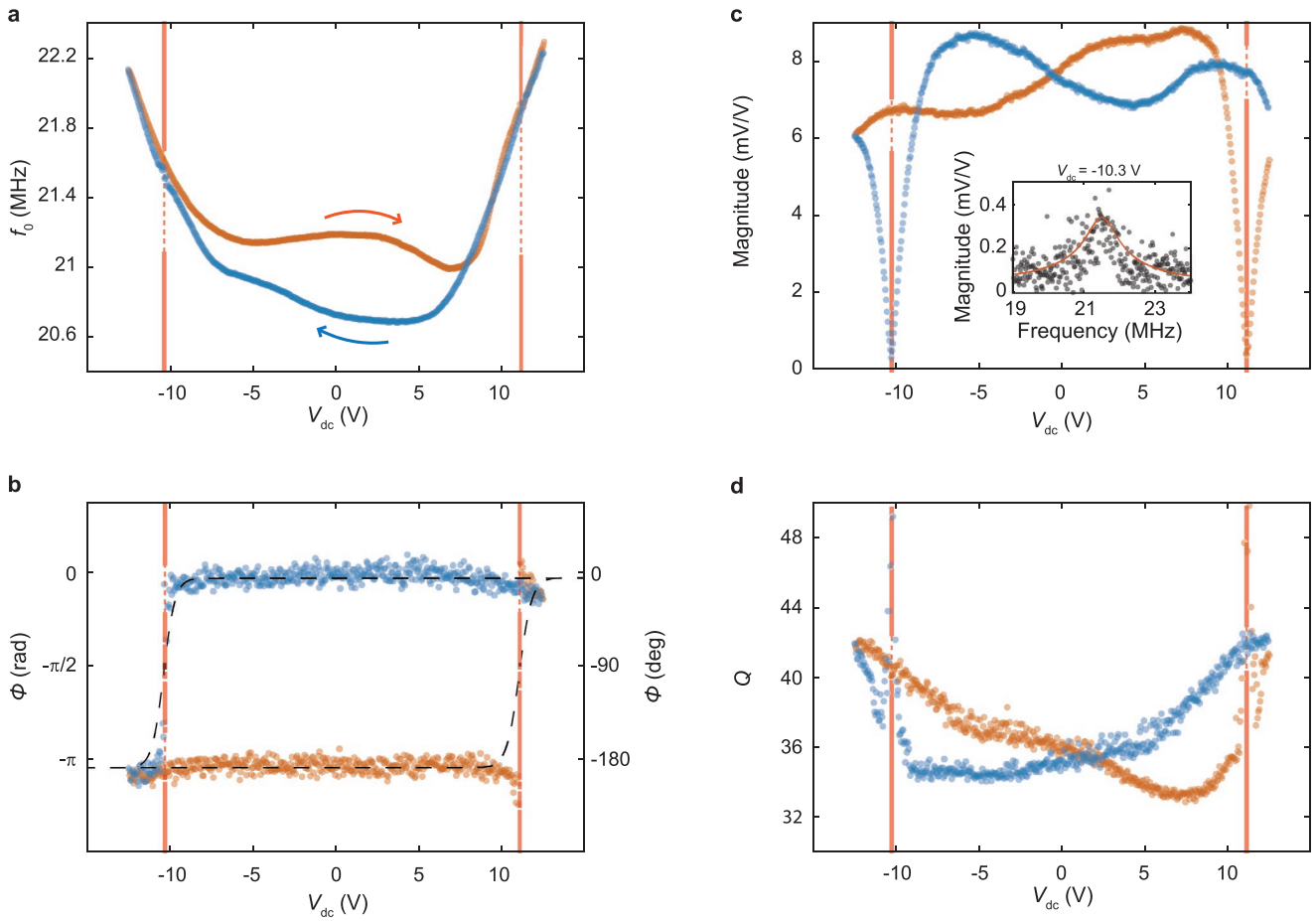

Figure 3. Ferroelectric hysteresis observed in the mechanical observables during a V_{DC} sweep (red and blue data correspond to upward and downward sweep respectively). a) Fundamental resonance frequency f_0. b) Phase ϕ when driving at resonance and a hyperbolic tangent (black dashed lines) fit. c) Magnitude of the harmonic oscillator at its fundamental resonance frequency. Inset: example of the measured magnitude of resonance peak (gray dots) at the coercive field, $V_{DC} = -10.3$ V and a harmonic oscillator fit (solid line). d) Mechanical Q-factor. In all plots, orange traces are taken while increasing the DC bias and the blue traces are taken while decreasing the DC bias. Vertical red dashed lines denote the positions of the coercive fields. An actuation voltage of $V_{AC} = 10$ mV is used for the measurements displayed in panels (a–d). Errors from fits are smaller than the marker sizes everywhere except at the coercive field for f_0, magnitude and Q. The standard error in ϕ is smaller than 0.45 rad.

It is worth noting the discrepancy between the coercive field observed in the mechanics of the heterostructure and that found in the PFM data (see Section S2, Supporting Information). The coercive field observed in the mechanics (≈10.5 V) is nearly a factor of 10 higher than that observed in the PFM (≈0.86 V). There may be multiple causes for this discrepancy such as a "dead layer" often observed in ferroelectric materials,[44–46] local nucleation of low quality crystal[3] and the contaminations at the graphene-BTO interface which contribute toward a lower net capacitance. Since the stacking of the layers is performed in air, and subsequent chemical treatments to remove the polymer residues is avoided to prevent the collapse of the membrane, the interface likely has trapped hydrocarbons, polymers and/or air, effectively adding a low κ capacitor in series to the BTO (i.e., $C_{tot}^{-1} = C_{BTO}^{-1} + C_{interface}^{-1}$) thereby reducing the total capacitance and electric fields in the piezoelectric layer. Therefore, a higher voltage is required to reach the coercive electric field across the BTO flake in device 1.

In device 2 however, the coercive fields are comparable to those observed in the PFM data. **Figure 4**a shows the magnitude of the resonance peak as a function of DC bias, which qualitatively matches well the displacement data from the PFM measurement in Figure 4b. Agreement in the coercive fields measured by mechanics and PFM can be ascribed to a negligible $C_{interface}^{-1}$ in device 2 where all the voltage drop is across the BTO flake, that is, $C_{tot} \approx C_{BTO}$. The voltage dependence of the resonance frequency and its derivative with respect to the DC bias voltage can be found in Section S5, Supporting Information.

Frequency tunability is a powerful functionality that is expected to help reduce device real-estate in smart devices.[47] Tunable-frequency and reconfigurable multiband FBAR filters can replace multiple, fixed-frequency filters that are needed to select the right RF frequency at the antenna of mobile devices. This does not only reduce system size and cost, but also avoids electrical signal losses in switches that are needed to enable reconfigurability with fixed frequency filters.[48] Therefore, the frequency tunability—which can be engineered at the device level—as observed in our ferroelectric actuator (Figure 3a) is a highly sought after property in piezoelectric resonator devices.

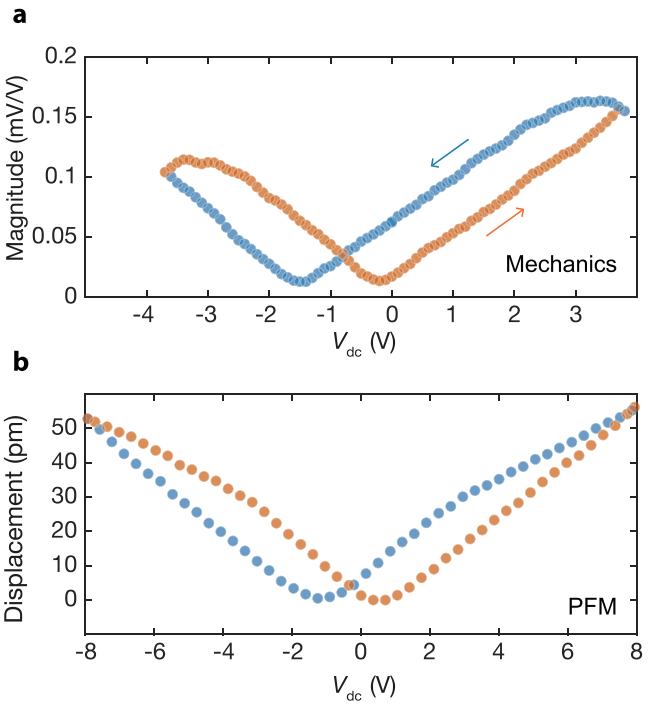

Figure 4. Comparison between the hysteresis from the mechanics and PFM measurements. a) Magnitude data at the resonance frequency from the mechanics of device 2. b) Displacement data from the PFM measurement of bare BTO. The orange traces are taken while increasing the DC bias and the blue traces are taken while decreasing the DC bias.

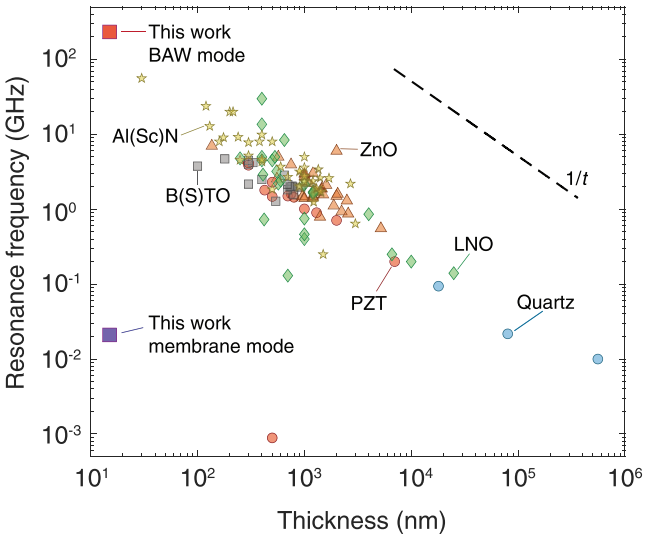

Figure 5. Piezoelectric actuators and filters of different chemical compositions (yellow star: Al(Sc)N, gray square: B(S=Sr)TO, orange triangle: ZnO, green diamond: $LiNbO_3$ (LNO), red circle: PZT, blue hexagon: quartz) plotted with their thickness and resonance frequency. The membrane mode of this work is shown as a purple square and the bulk acoustic wave resonance measured via picosecond ultrasonics measurements as a red square. The dashed black line is the plot of the thickness dependence of the resonance frequency, $f_{resonance} \propto 1/t$ for visual aid. The list of references for corresponding works can be found in the Supporting Information. Note that the *x*-axis only accounts for the piezoelectric layer thickness whereas the electrode thickness should also be minimized.

Instrumental limitations (i.e., frequency limit of our vector network analyzer, VNA and the optical detector) prohibited us to observe the existence of the bulk acoustic mode with laser interferometry. Therefore we use an optical pump–probe method called picosecond ultrasonics to probe the BAW mode of our devices. Using a pump laser of $\lambda = 1560$ nm and a probe laser of $\lambda = 780$ nm, we optically excite acoustic pulses on the electrodes of the heterostructure. See ref. [12] for experimental details. Results of the picosecond ultrasonics measurements are presented in Section S9, Supporting Information. Acoustic echoes reflecting off of the top/bottom surfaces of the heterostructure are measured with the probe laser after some time delay. Oscillations with a period of 4.3 ps are observed which corresponds to 233 GHz in both device 1 and device 3. The FBAR frequency is estimated as $f_{FBAR} = c_s / 2t$, where c_s is the speed of sound and $t = 14.7$ nm the thickness. From this the speed of sound can be estimated as 6850 m s^{-1} which is comparable to that of bulk BTO.[49]

Although we were limited by our instruments, we predict that a high-frequency VNA with a frequency upconverter may be able to reach high enough frequencies to also be able to electrically verify the $f_{FBAR} = 233$ GHz of our devices. Recently, Kim et al.[50] have experimentally demonstrated the viability of MoS_2 up to 480 GHz using their high-frequency VNA and home-built frequency upconverters. Such setup may be more suitable in an industrial setting to verify the f_{FBAR} of individual devices.

The work reported here showcases—to the best of our knowledge—the thinnest suspended piezoelectric resonator reported to date with the highest f_{FBAR}. **Figure 5** displays a collection of piezoelectric resonators reported in literature, with the resonance frequency of the piezoelectric layer versus its thickness of the piezoelectric layer as a figure of merit. Most devices have piezoelectric layers in the $t \approx 100$ nm to 10 µm range, with the presented device ($t = 14.7$ nm) being substantially thinner than the thinnest BAW resonator reported thus far in the work by Tanifuji et al.,[51] who report on the fabrication and simulation of a resonator made of 30 nm thick piezoelectric material (AlN) contacted by Ru electrodes of 40 nm in thickness, with an expected resonance frequency of 56 GHz. Corresponding references can be found in Section S10, Supporting Information.

In this work, the thickness of the graphite electrodes is not reduced to the monolayer limit, in order to clearly demonstrate the piezoelectric actuation. By making the bottom electrode sufficiently thick to screen the electric field originating from the top electrode, we prevent electrostatic actuation from playing a role in the piezoelectric actuation when the bottom electrode is grounded. However, after we establish the piezoelectric actuation in this work, future devices can be composed of monolayer graphene electrodes. Since graphene conducts electricity down to the monolayer limit and still supports high (>300 GHz) frequencies,[21] monolayer graphene is the ultimate electrode material for ultrathin piezoelectric resonators. Similarly, the thickness of the BTO used in this work (36 u.c.) can be further reduced to improve the f_{FBAR} further. Ji et al.[52] demonstrated the possibility of having single unit cell freestanding complex oxides and the retention of ferroelectricity in 3 u.c. $BiFeO_3$. Taking into account the destructiveness of electron tunneling, dielectric breakdown and the reduction of the

piezoelectric properties at the ultrathin limit,[53,54] BTO flakes could potentially be thinned down to the several-unit-cells limit making the total thickness of the device thinner than 5 nm and $f_{FBAR} > 600$ GHz.

Lead zirconate titanate (PZT) is a well established high performance perovskite piezoelectric which can also be epitaxially grown and released into the free-standing form.[55] Due to its ultrahigh piezoelectric constant, it has been widely adopted in applications that require piezoelectric properties for many decades leading up to the early 2000s. However, in 2003, the European Union published its plan to restrict the use of hazardous materials such as Pb and Cr-6 in electronic devices which later came in action in 2006.[56] Therefore, there is a huge pressure to switch from lead-based piezoelectrics to lead-free ones in the industry. One of the candidate materials to replace PZT is BTO. BTO is a lead-free piezoelectric with comparably high d_{33} which still maintains ferro/piezoelectric properties at room temperature. We anticipate that the ferroelectric properties of BTO can be further engineered by controlling the concentration of Sr in BSTO.[57]

3. Conclusion

We have demonstrated a device geometry composed of ultrathin free-standing complex oxides interfaced with van der Waals electrodes and assessed its potential use in next-generation telecommunication applications. We used a free-standing, lead-free ferroelectric, $BaTiO_3$ in an FBAR geometry with graphene as electrodes. Optothermal, electrostatic, and piezoelectric actuation methods were explored to compare the mechanical behavior of the heterostructure. Unlike the electrostatically driven state, the piezoelectrically driven state shows clear hysteresis in the mechanical parameters f_0, Q, ϕ, and magnitude. The BAW mode measured at 233 GHz is the highest reported and is situated in 6G frequencies. Our work establishes vdW-material–complex-oxide heterostructures as a promising route to enable agile resonators, engineered at the atomic scale, with improved performances.

4. Experimental Section

PLD Growth of Free-Standing BTO: $BaTiO_3$ was grown on a water soluble sacrificial layer, $Sr_3Al_2O_6$, which was grown on a $SrTiO_3$ (001) single-crystal substrate with TiO_2 termination. $Sr_3Al_2O_6$ was grown in 4×10^{-6} mbar at 725 °C with a excimer laser fluence of 1.2 J cm^{-2} pulsed at 1 Hz. $BaTiO_3$ was grown in 2×10^{-6} mbar at 650 °C with a fluence of 1 J cm^{-2} pulsed at 1 Hz. After growth, the samples were annealed at 550 °C in an oxygen pressure of 300 mbar for 1 h and slowly cooled down to room temperature at 20 °C min^{-1}.

Characterization of Free-Standing BTO: PFM was performed using an Asylum Cypher atomic force microscopy (AFM). A flake of free standing $BaTiO_3$ was stamped on a prepatterned gold electrode on SiO_2/Si which was grounded. A metal coated MFMV cantilever was brought in contact with the $BaTiO_3$ flake and was used to apply an electric field to the flake while monitoring the deflection of the cantilever. XRD was performed using Bruker Dimension D8 on epitaxially grown $BaTiO_3$/$Sr_3Al_2O_6$/$SrTiO_3$ and after the film was released onto SiO_2/Si. AFM in tapping mode was performed using an Asylum Cypher AFM or a Bruker Icon AFM.

Fabrication of Pre-Patterned Substrates: Thermally grown SiO_2 on Si was used as a starting substrate. Electrode patterns were exposed with a Raith EBPG-5000+ using a poly(methyl methacrylate) (PMMA) 950k–495k bilayer as a resist. After development, SiO_2 was slightly etched in a Sentech Etchlab 200 reactive ion etcher (RIE) with a plasma composed of CHF_3 and Ar. The electrodes were then metallized with Ti and Pd using an AJA e-beam evaporation system. The cavities were defined by exposing the design in an AR-P 6200 e-beam resist using the EBPG-5000+. After development, Sentech Etchlab 200 RIE was used to etch the exposed SiO_2 all the way to the Si.

Fabrication of Van der Waals Heterostructure: Dry transfer of top and bottom graphene layers were performed using the deterministic PDMS transfer method,[31] with home-made PDMS stamps and scotch tape. Free standing $BaTiO_3$ flakes were transferred with polypropylene carbonate (PPC) layers[34] spin coated on PDMS domes.[35] The bottom graphene layer was transferred with bare PDMS and $BaTiO_3$ was transferred on top of the bottom graphene layer using the PPC/PDMS dome. Residual PPC was annealed in ambient conditions at 300 °C for 10 min in the case of device 1, and 1 h for device 2. Finally, the top graphene layer was again transferred using the bare PDMS method.

Actuation and Interferometry: Optothermal actuation was performed by shining an intensity modulated blue (λ = 405 nm) laser onto the membrane. Electrostatic actuation was performed by driving the Si back gate with an AC signal on top of a DC offset while the top and bottom graphene were grounded. Piezoelectric actuation was realized by sending an AC signal on top of a DC offset onto the top graphene electrode while the bottom graphene and the Si were grounded. In all of these actuations, the output of a Rohde&Schwarz vector network analyzer was used as the AC source and the DC offset was provided by a Keysight B2901A source measure unit. Interferometry was performed with a red (λ = 633 nm) He–Ne laser which was focused on the membrane using a 50× objective after passing through a quarter wave plate. The reflected red laser passed through the quarter wave plate again and was reflected off of a polarization beam splitter onto a photodetector. This signal was collected at the input of the vector network analyzer.

Picosecond Ultrasonics: Picosecond ultrasonics measurements were performed using an asynchronous optical sampling system (ASOPS) from Menlo Systems. Acoustic pulses were generated by locally heating the metallic (absorptive) part of the heterostructure (graphite) using a 100 fs pump pulse generated with a femtosecond erbium laser (λ = 1560 nm), which was doubled in frequency (λ = 780 nm) for the probe laser. The probe pulse measured the acoustic echoes that were reflected from the boundaries of the heterostructure with the repetition rate at a slight offset from the 100 MHz pump, regulated by ASOPS. See ref. [12] for detailed description of the method.

Supporting Information

Supporting Information is available from the Wiley Online Library or from the author.

Acknowledgements

M.L., M.Š., H.S.J.v.d.Z. and P.G.S. acknowledge funding from the European Union's Horizon 2020 research and innovation program under grant agreement number 881603. E.L. acknowledges funding from the EU Horizon 2020 research and innovation programme under the Marie Skłodowska-Curie grant agreement no. 707404. A.D.C. acknowledges funding from Quantox of QuantERA ERA-NET Cofund in Quantum Technologies and by the Netherlands Organisation for Scientific Research (NWO/OCW) as part of the VIDI program. G.J.V. acknowledges support from project TKI-HTSM/19.0172.

Conflict of Interest

The authors declare no conflict of interest.

Data Availability Statement

The data that support the findings of this study are openly available in Zenodo at https://doi.org/10.5281/zenodo.7022717.

Keywords

2D materials, actuators, complex oxides, ferroelectrics, nano-electromechanical systems, piezoelectrics, resonators

Received: May 23, 2022
Revised: August 27, 2022
Published online:

[1] Y. Liu, Y. Cai, Y. Zhang, A. Tovstopyat, S. Liu, C. Sun, *Micromachines* **2020**, *11*, 630.
[2] L. Lian, N. R. Sottos, *J. Appl. Phys.* **2000**, *87*, 3941.
[3] J. Y. Jo, Y. S. Kim, T. W. Noh, J.-G. Yoon, T. K. Song, *Appl. Phys. Lett.* **2006**, *89*, 232909.
[4] M. Yoshimura, H. K. Bowen, *J. Am. Ceram. Soc.* **1981**, *64*, 404.
[5] S. I. Shkuratov, J. Baird, E. F. Talantsev, *Appl. Phys. Lett.* **2013**, *102*, 052906.
[6] J. J. Wang, Z. Z. He, C. Yu, X. B. Song, H. X. Wang, F. Lin, Z. H. Feng, *Diamond Relat. Mater.* **2016**, *70*, 114.
[7] V. Harbola, S. Crossley, S. S. Hong, D. Lu, Y. A. Birkholzer, Y. Hikita, H. Y. Hwang, *Nano Lett.* **2021**, *21*, 2470.
[8] S. S. Hong, M. Gu, M. Verma, V. Harbola, B. Y. Wang, D. Lu, A. Vailionis, Y. Hikita, R. Pentcheva, J. M. Rondinelli, H. Y. Hwang, *Science* **2020**, *368*, 71.
[9] R. Xu, J. Huang, E. S. Barnard, S. S. Hong, P. Singh, E. K. Wong, T. Jansen, V. Harbola, J. Xiao, B. Y. Wang, S. Crossley, D. Lu, S. Liu, H. Y. Hwang, *Nat. Commun.* **2020**, *11*, 3141.
[10] V. Harbola, R. Xu, S. Crossley, P. Singh, H. Y. Hwang, *Appl. Phys. Lett.* **2021**, *119*, 053102.
[11] B. Peng, R.-C. Peng, Y.-Q. Zhang, G. Dong, Z. Zhou, Y. Zhou, T. Li, Z. Liu, Z. Luo, S. Wang, Y. Xia, R. Qiu, X. Cheng, F. Xue, Z. Hu, W. Ren, Z.-G. Ye, L.-Q. Chen, Z. Shan, T. Min, M. Liu, *Sci. Adv.* **2020**, *6*, eaba5847.
[12] M. Lee, M. Robin, R. Guis, U. Filippozzi, D. H. Shin, T. C. van Thiel, S. Paardekooper, J. R. Renshof, H. S. J. van der Zant, A. D. Caviglia, G. J. Verbiest, P. G. Steeneken, *Nano Lett.* **2022**, *22*, 1475.
[13] D. Davidovikj, D. J. Groenendijk, A. M. R. V. L. Monteiro, A. Dijkhoff, D. Afanasiev, M. Šiškins, M. Lee, Y. Huang, E. van Heumen, H. S. J. van der Zant, A. D. Caviglia, P. G. Steeneken, *Commun. Phys.* **2020**, *3*, 163.
[14] N. Manca, G. Mattoni, M. Pelassa, W. J. Venstra, H. S. J. van der Zant, A. D. Caviglia, *ACS Appl. Mater. Interfaces* **2019**, *11*, 44438.
[15] K. S. Novoselov, A. K. Geim, S. V. Morozov, D.-e. Jiang, Y. Zhang, S. V. Dubonos, I. V. Grigorieva, A. A. Firsov, *Science* **2004**, *306*, 666.
[16] K. I. Bolotin, K. J. Sikes, Z. Jiang, M. Klima, G. Fudenberg, J. Hone, P. Kim, H. Stormer, *Solid State Commun.* **2008**, *146*, 351.
[17] L. Banszerus, M. Schmitz, S. Engels, M. Goldsche, K. Watanabe, T. Taniguchi, B. Beschoten, C. Stampfer, *Nano Lett.* **2016**, *16*, 1387.
[18] C. Lee, X. Wei, J. W. Kysar, J. Hone, *Science* **2008**, *321*, 385.
[19] M. Lee, D. Davidovikj, B. Sajadi, M. Šiškins, F. Alijani, H. S. J. van der Zant, P. G. Steeneken, *Nano Lett.* **2019**, *19*, 5313.
[20] H. H. Pérez Garza, E. W. Kievit, G. F. Schneider, U. Staufer, *Nano Lett.* **2014**, *14*, 4107.
[21] Y. Wu, K. A. Jenkins, A. Valdes-Garcia, D. B. Farmer, Y. Zhu, A. A. Bol, C. Dimitrakopoulos, W. Zhu, F. Xia, P. Avouris, Y.-M. Lin, *Nano Lett.* **2012**, *12*, 3062.
[22] Q. Zhou, J. Zheng, S. Onishi, M. Crommie, A. K. Zettl, *Proc. Natl. Acad. Sci. USA* **2015**, *112*, 8942.
[23] D. Todorović, A. Matković, M. Milićević, D. Jovanović, R. Gajić, I. Salom, M. Spasenović, *2D Mater.* **2015**, *2*, 045013.
[24] Q. Zhou, A. Zettl, *Appl. Phys. Lett.* **2013**, *102*, 223109.
[25] M. Šiškins, M. Lee, D. Wehenkel, R. van Rijn, T. W. de Jong, J. R. Renshof, B. C. Hopman, W. S. Peters, D. Davidovikj, H. S. J. van der Zant, P. G. Steeneken, *Microsyst. Nanoeng.* **2020**, *6*, 102.
[26] I. E. Rosłoń, A. Japaridze, P. G. Steeneken, C. Dekker, F. Alijani, *Nat. Nanotechnol.* **2022**, *17*, 637.
[27] R. Pezone, G. Baglioni, P. M. Sarro, P. G. Steeneken, S. Vollebregt, *ACS Appl. Mater. Interfaces* **2022**.
[28] S. Wittmann, C. Glacer, S. Wagner, S. Pindl, M. C. Lemme, *ACS Appl. Nano Mater.* **2019**, *2*, 5079.
[29] X. Fan, F. Forsberg, A. D. Smith, S. Schröder, S. Wagner, H. Rödjegård, A. C. Fischer, M. Östling, M. C. Lemme, F. Niklaus, *Nat. Electron.* **2019**, *2*, 394.
[30] D. Lu, D. J. Baek, S. S. Hong, L. F. Kourkoutis, Y. Hikita, H. Y. Hwang, *Nat. Mater.* **2016**, *15*, 1255.
[31] A. Castellanos-Gomez, M. Buscema, R. Molenaar, V. Singh, L. Janssen, H. S. van der Zant, G. A. Steele, *2D Mater.* **2014**, *1*, 011002.
[32] Y. Matsubara, K. S. Takahashi, Y. Tokura, M. Kawasaki, *Appl. Phys. Express* **2014**, *7*, 125502.
[33] K. P. Kelley, D. E. Yilmaz, L. Collins, Y. Sharma, H. N. Lee, D. Akbarian, A. C. T. Van Duin, P. Ganesh, R. K. Vasudevan, *Phys. Rev. Mater.* **2020**, *4*, 024407.
[34] F. Pizzocchero, L. Gammelgaard, B. S. Jessen, J. M. Caridad, L. Wang, J. Hone, P. Bøggild, T. J. Booth, *Nat. Commun.* **2016**, *7*, 11894.
[35] K. Kim, M. Yankowitz, B. Fallahazad, S. Kang, H. C. Movva, S. Huang, S. Larentis, C. M. Corbet, T. Taniguchi, K. Watanabe, S. K. Banerjee, B. J. LeRoy, E. Tutuc, *Nano Lett.* **2016**, *16*, 1989.
[36] J. Lee, Z. Wang, K. He, R. Yang, J. Shan, P. X.-L. Feng, *Sci. Adv.* **2018**, *4*, eaao6653.
[37] C. Chen, Ph.D. Thesis, Columbia University, New York **2013**.
[38] M. Šiškins, M. Lee, S. Mañas-Valero, E. Coronado, Y. M. Blanter, H. S. J. van der Zant, P. G. Steeneken, *Nat. Commun.* **2020**, *11*, 2698.
[39] M. E. Lines, A. M. Glass, *Principles and Applications of Ferroelectrics and Related Materials*, Oxford University Press, Oxford, UK **2001**.
[40] U. K. Bhaskar, N. Banerjee, A. Abdollahi, Z. Wang, D. G. Schlom, G. Rijnders, G. Catalan, *Nat. Nanotechnol.* **2016**, *11*, 263.
[41] R. C. Smith, C. L. Hom, *J. Intell. Mater. Syst. Struct.* **1999**, *10*, 195.
[42] C. Stefani, L. Ponet, K. Shapovalov, P. Chen, E. Langenberg, D. G. Schlom, S. Artyukhin, M. Stengel, N. Domingo, G. Catalan, *Phys. Rev. X* **2020**, *10*, 041001.
[43] L. You, Y. Zhang, S. Zhou, A. Chaturvedi, S. A. Morris, F. Liu, L. Chang, D. Ichinose, H. Funakubo, W. Hu, T. Wu, Z. Liu, S. Dong, J. Wang, *Sci. Adv.* **2019**, *5*, eaav3780.
[44] Y. Gagou, J. Belhadi, B. Asbani, M. El Marssi, J.-L. Dellis, Y. I. Yuzyuk, I. P. Raevski, J. F. Scott, *Mater. Des.* **2017**, *122*, 157.
[45] L.-W. Chang, M. Alexe, J. F. Scott, J. M. Gregg, *Adv. Mater.* **2009**, *21*, 4911.
[46] X. L. Li, B. Chen, H. Y. Jing, H. B. Lu, B. R. Zhao, Z. H. Mai, Q. J. Jia, *Appl. Phys. Lett.* **2005**, *87*, 222905.
[47] K.-y. Hashimoto, S. Tanaka, M. Esashi, in *2011 Joint Conf. of the IEEE Int. Frequency Control and the European Frequency and Time*

Forum (FCS) Proc., IEEE, Piscataway, NJ, USA **2011**, https://doi.org/10.1109/FCS.2011.5977297.

[48] K. R. Boyle, P. G. Steeneken, *IEEE Trans. Antennas Propag.* **2007**, *55*, 3300.

[49] S. Kashida, I. Hatta, A. Ikushima, Y. Yamada, *J. Phys. Soc. Jpn.* **1973**, *34*, 997.

[50] M. Kim, G. Ducournau, S. Skrzypczak, S. J. Yang, P. Szriftgiser, N. Wainstein, K. Stern, H. Happy, E. Yalon, E. Pallecchi, D. Akinwande, *Nat. Electron.* **2022**, *5*, 367.

[51] S. Tanifuji, Y. Aota, S. Kameda, T. Takagi, K. Tsubouchi, in *2009 IEEE Int. Ultrasonics Symp.*, IEEE, Piscataway, NJ, USA **2009**, pp. 2170–2173.

[52] D. Ji, S. Cai, T. R. Paudel, H. Sun, C. Zhang, L. Han, Y. Wei, Y. Zang, M. Gu, Y. Zhang, W. Gao, H. Huyan, W. Guo, D. Wu, Z. Gu, E. Y. Tsymbal, P. Wang, Y. Nie, X. Pan, *Nature* **2019**, *570*, 87.

[53] E. Yarar, V. Hrkac, C. Zamponi, A. Piorra, L. Kienle, E. Quandt, *AIP Adv.* **2016**, *6*, 075115.

[54] K.-m. Zhang, Y.-p. Zhao, F.-q. He, D.-q. Liu, *Chin. J. Chem. Phys.* **2007**, *20*, 721.

[55] S. R. Bakaul, J. Kim, S. Hong, M. J. Cherukara, T. Zhou, L. Stan, C. R. Serrao, S. Salahuddin, A. K. Petford-Long, D. D. Fong, M. V. Holt, *Adv. Mater.* **2020**, *32*, 1907036.

[56] Directive 2002/95/EC of the European Parliament and of the Council of 27 January 2003 on the restriction of the use of certain hazardous substances in electrical and electronic equipment **2003**, https://eur-lex.europa.eu/LexUriServ/LexUriServ.do?uri=OJ:L:2003:037:0019:0023:en:PDF (accessed: July 2022).

[57] N. Ortega, A. Kumar, O. Resto, O. Maslova, Y. I. Yuzyuk, J. Scott, R. S. Katiyar, *J. Appl. Phys.* **2013**, *114*, 104102.